Weak Electron Phonon Coupling and Deep Level Impurity for High Thermoelectric Performance $Pb_{1-x}Ga_xTe$

Xianli Su, Shiqiang Hao, Trevor P. Bailey, Si Wang, Ido Hadar, Gangjian Tan, Tze-Bin Song, Qingjie Zhang, Ctirad Uher, Chris Wolverton, Xinfeng Tang, and Mercouri G. Kanatzidis**

High *ZT* of 1.34 at 766 K and a record high average *ZT* above 1 in the temperature range of 300-864 K are attained in n-type PbTe by engineering the temperature-dependent carrier concentration and weakening electron–phonon coupling upon Ga doping. The experimental studies and first principles band structure calculations show that doping with Ga introduces a shallow level impurity contributing extrinsic carriers and imparts a deeper impurity level that ionizes at higher temperatures. This adjusts the carrier concentration closer to the temperature-dependent optimum and thus maximizes the power factor in a wide temperature range. The maximum power factor of 35 μW cm^{-1} K^{-2} is achieved for the $Pb_{0.98}Ga_{0.02}Te$ compound, and is maintained over 20 μWcm^{-1} K^{-2} from 300 to 767 K. Band structure calculations and X-ray photoelectron spectroscopy corroborate the amphoteric role of Ga in PbTe as the origin of shallow and deep levels. Additionally, Ga doping weakens the electron–phonon coupling, leading to high carrier mobilities in excess of 1200 cm^2 V^{-1} s^{-1}. Enhanced point defect phonon scattering yields a reduced lattice thermal conductivity. This work provides a new avenue, beyond the conventional shallow level doping, for further improving the average *ZT* in thermoelectric materials.

1. Introduction

Thermoelectric materials, directly converting heat into electricity and vice versa, have attracted worldwide attention.[1] The conversion efficiency of thermoelectric materials is determined by the dimensionless figure of merit $ZT = S^2\sigma T/(\kappa_e + \kappa_L)$, where S is the Seebeck coefficient, σ is the electrical conductivity, T is the absolute temperature, and κ_e and κ_L are the electronic and lattice contributions to the thermal conductivity, respectively. Thus, an excellent thermoelectric material should simultaneously have a large Seebeck coefficient, high electrical conductivity, and a low lattice thermal conductivity.[2] Since all transport parameters are interdependent, achieving a high *ZT* is extremely difficult. It should be mentioned that, for practical applications, the efficiency of a thermoelectric device is determined by the average *ZT* of the material over the entire working temperature range instead of its maximum *ZT* value at a single temperature. Therefore, in power generation applications, it is the average *ZT* over a broad temperature range that must be maximized. Tremendous efforts have been devoted to tailoring the coupling among the transport parameters to improve thermoelectric properties.[3] Extensive experimental and theoretical investigations have demonstrated that high thermoelectric figure of merit can be achieved by a two-pronged strategy. One is to lower the thermal conductivity through the introduction of structural complexities that span from atomic scale to mesoscale, such as forming solid solutions to enhance alloy phonon scattering and developing nanostructures to increase interfacial phonon scattering.[2b,3a,4] However, for a specific solid, the thermal conductivity has a theoretical lower limit, the so-called amorphous limit, when the mean free path of phonons equals the shortest interatomic distance.[5] The second strategy to boost the figure of merit is of purely electronic nature and consists of modulating the power factor, which is determined by the electronic band structure and scattering mechanisms, via, for example, an introduction of band resonant levels, an adjustment of the band edge locations, and arranging for a charge carrier energy filtering effect.[4f,k,6] It should be noted that all the above

Dr. X. Su, S. Wang, Prof. Q. Zhang, Prof. X. Tang
State Key Laboratory of Advanced Technology for Materials Synthesis and Processing
Wuhan University of Technology
Wuhan 430070, China
E-mail: tangxf@whut.edu.cn

Dr. X. Su, Dr. I. Hadar, Dr. G. Tan, Dr. T.-B. Song, Prof. M. G. Kanatzidis
Department of Chemistry
Northwestern University
Evanston, IL 60208, USA
E-mail: m-kanatzidis@northwestern.edu

Dr. S. Hao, Prof. C. Wolverton, Prof. M. G. Kanatzidis
Department of Materials Science and Engineering
Northwestern University
Evanston, IL 60208, USA

T. P. Bailey, S. Wang, Prof. C. Uher
Department of Physics
University of Michigan
Ann Arbor, MI 48109, USA

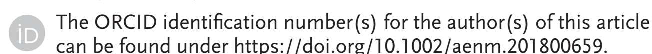
The ORCID identification number(s) for the author(s) of this article can be found under https://doi.org/10.1002/aenm.201800659.

DOI: 10.1002/aenm.201800659

© 2018 WILEY-VCH Verlag GmbH & Co. KGaA, Weinheim

strategies and the enhancement in *ZT* are achieved with a tacit precondition of the optimized carrier concentration. However, for a given material, the carrier concentration that produces the largest thermoelectric figure of merit is not constant in the whole temperature range and is always a function of the temperature. For example, assuming single band conduction and using the classical statistics equations as a rough approximation, the optimum carrier concentration n^* for a given material depends on the temperature as $n^* \sim T^{1.5}$, indicating that a higher carrier concentration is required for maximizing the power factor at higher temperatures.[7] This poses a challenge for optimizing the average *ZT* of the materials, since conventional doping usually introduces impurity levels close to the band edge, called shallow level impurities, which are ionized at very low temperatures. As a result, the carrier concentration is almost constant in the extrinsic region.[8] Although the carrier concentration increases rapidly in the intrinsic regime of conduction, the thermally excited electron–hole pairs not only increase the bipolar contribution to the thermal conductivity but also diminish the Seebeck coefficient, resulting in a significant reduction of *ZT*.[9] It is well known that deep level impurity states, which are considered to be separated by at least 100 meV from the band edge, require higher thermal energy and thereby a higher temperature to be ionized in comparison with shallow level impurity states.[8,10] Therefore, deep level impurity states can contribute additional charge carriers at elevated temperatures, allowing for the tuning of the carrier concentration closer to its optimum value over a broader temperature range. In addition, the deep level impurity ionization increases the population of the majority carrier, shifting the onset of undesirable intrinsic excitations to higher temperatures. In both cases, this is beneficial for the high average *ZT* and the improved maximum efficiency. However, so far, very little systematic work has been reported focusing on the effects of deep level impurities on thermoelectric properties.[8a]

Since Ga has long been considered as a deep level dopant in the PbTe system, we chose it as an example to investigate the effect of a deep level impurity on the thermoelectric properties, aided by ab initio calculations and experimental studies. A series of Ga-doped $Pb_{1-x}Ga_xTe$ (x = 0–0.035) compounds were synthesized by vacuum melting-annealing combined with the spark plasma sintering (SPS) process, and the effect of Ga doping on the band structure and the thermoelectric properties of $Pb_{1-x}Ga_xTe$ was assessed. Our computational and experimental results demonstrate that Ga doping on the Pb site forms deep impurity levels in the electronic band structure via the Ga 4s orbitals corresponding to the Ga^{1+} valence state, while the Ga^{3+} states act as a shallow level impurity. Compared to the Ga^{3+} impurity that is already ionized at low temperatures, the deep impurity levels of Ga^{1+} ionize at temperatures above 473 K, contributing additional electrons and tuning the temperature-dependent carrier concentration at these elevated temperatures. The dual nature of the dopant allows for an additional knob to maintain the carrier concentration closer to the optimal value required for maximizing the power factor over a wider temperature range. In addition, Ga doping enhances point defect phonon scattering and decreases the lattice thermal conductivity. All these factors are beneficial for achieving a high average *ZT* in the measured temperature range. The highest *ZT* of 1.34 was obtained at 766 K for $Pb_{0.98}$ $Ga_{0.02}Te$, while at the same time resulting in a record high average *ZT* of 1.12 between 420 and 865 K.

2. Results and Discussion

2.1. Electronic and Structural Properties

To explore the deep level impurity states in Ga-doped $Pb_{1-x}Ga_xTe$ compounds, we used 3 × 3 × 3 times of the PbTe primitive cell, forming a supercell of $Pb_{27}Te_{27}$ and then calculated the electronic band structure of $Pb_{27-x}Ga_xTe_{27}$ (x = 0, 1) compounds in the rock salt structure (**Figure 1**a–c). Clearly, compared to pure PbTe, there are impurity states in the gap around the Fermi level, which are from Ga 4s and Ga 4p hybridization with Pb 6p and Te 5p states, as shown in the band structure and projected density of states. It is necessary to mention that in the Ga-doped PbTe system, as shown in the electronic DOS figure, the energy corresponding to the red peak from Ga 4p is higher than that of the green peak from Ga 4s, suggesting the Ga 4s state is slightly more tightly bound and lies below the valence 4p state. In this sense, the Ga 4p electron is more easily transferred to the Te 5p band. Due to a relatively higher energy of the Ga 4p state, two Ga impurities, after each donating one electron to the Te 5p band, form $2Ga^{2+}$, which dissociates into Ga^{+} and Ga^{3+}, forming a mix valence state of the Ga dopant. Similar phenomenon has been observed in In-doped PbTe.[11] The trivalent In substituted for divalent Pb in PbTe will create an n-type donor by giving two electrons by two In impurities with each donating one electron to fill the valence band, which is predominantly Te 5p hybridized with Pb 6p. But, due to the In 5s state being lower in energy than the 5p state, two In impurities, after donating two electrons to the Te 5p band, form $2In^{2+}$, which in turn dissociates into In^{+} and In^{3+}, further pinning the Fermi level right in the middle of gap and showing an n-type conduction with very low extrinsic carrier concentration of ≈2.5×10^{18} cm^{-3}.[12] For the Ga-doped $Pb_{1-x}Ga_xTe$, the Fermi level pinning is also detected but with a relatively higher carrier concentration of ≈1×10^{19} cm^{-3}.

To further verify the presence of deep level impurity states in the $Pb_{1-x}Ga_xTe$ compounds, Figure 1d shows the temperature dependence of the Hall coefficient R_H for the Ga-doped $Pb_{0.98}Ga_{0.02}Te$ sample, divided into three regions based on the slope. The first region is the temperature interval of 300–473 K, the second region 473–723 K, and the third region 723–823 K, with a sharp change in the slope of R_H versus T observed between each region. In previous studies with La-doped PbTe[7a] and iodine-doped PbTe samples, the temperature-dependent R_H was similar to that of a conventional highly degenerate semiconductor. The Hall coefficient is independent of the temperature in the extrinsic transport regime, and in the intrinsic regime, the absolute value of R_H decreases significantly. The temperature-dependent Hall coefficient of the $Pb_{0.98}Ga_{0.02}Te$ sample seems to indicate the formation of a deep impurity level in the electronic band structure, as only above 473 K is the thermal energy sufficient to ionize such deep levels.

In order to reveal the chemical state and shed light on the formation mechanism of the deep level impurity, PbTe and

© 2018 WILEY-VCH Verlag GmbH & Co. KGaA, Weinheim

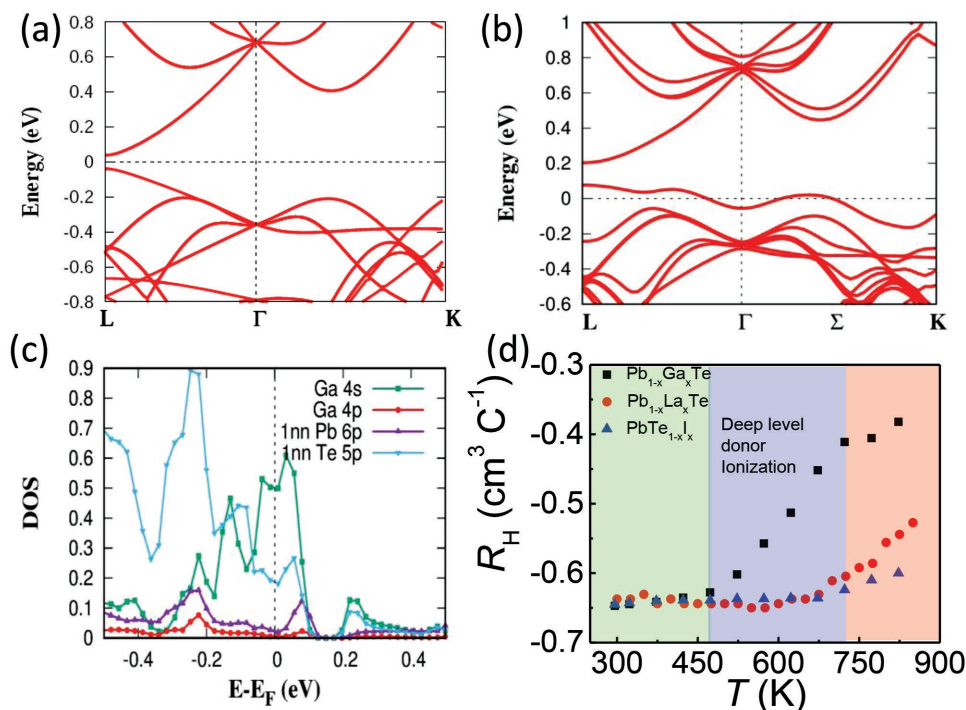

Figure 1. The calculated electronic band structures of $Pb_{27-x}Ga_xTe_{27}$ ($x = 0, 1$): a) $x = 0$; b) $x = 1$. Compared with pure PbTe, gap states in Ga-doped PbTe are induced from a hybridization of Ga 4s and Te 5p states. c) Contributions to the density of states of $Pb_{26}GaTe_{27}$ by the 6p orbital of Pb, 5p orbital of Te, 4s orbital of Ga, and 4p orbital of Ga; d) temperature dependence of Hall coefficient of $Pb_{1-x}Ga_xTe$. La-doped PbTe[7a] and I-doped PbTe both with the room temperature carrier concentration of 1×10^{19} cm^{-3} are also plotted for comparison.

$Pb_{0.98}Ga_{0.02}Te$ were selected as typical samples for X-ray photoelectron spectroscopy (XPS) measurements. **Figure 2**a shows photoemission spectra of Pb $4f_{7/2}$ and $4f_{5/2}$ core levels for PbTe and $Pb_{0.98}Ga_{0.02}Te$, and Figure 2b shows photoemission spectra of Te $3d_{5/2}$ and $3d_{3/2}$ core levels. The spectral peaks of Pb $4f_{7/2}$ and $4f_{5/2}$ core levels and Te $3d_{5/2}$ and $3d_{3/2}$ core levels of both samples are symmetric, indicating the expected valence states for both Pb and Te in PbTe and $Pb_{0.98}Ga_{0.02}Te$. Regardless of Ga content, no shifts in the peak position of Pb and Te are observed, indicating that the chemical environment of Pb and Te atoms in the $Pb_{1-x}Ga_xTe$ compounds has not changed. Binding energies of 137.4 and 142.2 eV correspond to Pb $4f_{7/2}$ and Pb $4f_{5/2}$, respectively. The spin–orbital components are separated by 4.8 eV, indicating the valence of Pb in $Pb_{1-x}Ga_xTe$ compounds is 2+. Te binding energies of 572.3 and 582.7 eV correspond to Te $3d_{5/2}$ and Te $3d_{3/2}$, respectively, giving the spin–orbital separation of 10.4 eV, and indicating that the valence of Te in $Pb_{1-x}Ga_xTe$ compounds is 2–. The deconvoluted spectra of the Ga $2p_{3/2}$ core level and Ga $2p_{1/2}$ are shown in Figure 2c,d, respectively. As reference, we have collected X-ray photoelectron spectra of Ga_2Te_3 where the valence of Ga is exclusively 3+. The peaks of Ga $2p_{3/2}$ and $2p_{1/2}$ core levels in the Ga_2Te_3 compound are symmetric and can be fitted by a single peak with the binding energy of 1117.8 and 1144.7 eV, respectively. In contrast, the peaks of Ga $2p_{3/2}$ and $2p_{1/2}$ core levels in the $Pb_{0.98}Ga_{0.02}Te$ compound are asymmetric and are much broader than in Ga_2Te_3, which indicates a mixture of valences in the $Pb_{0.98}Ga_{0.02}Te$ compound. From the deconvolution, the $Pb_{0.98}Ga_{0.02}Te$ sample has two chemical states in which the 1144.5 and 1117.6 eV peaks represent the Ga^{3+} state in PbTe, while the 1145.7 and 1118.8 eV peaks represent the Ga^{1+} state in PbTe. Evidently, Ga^{3+} is the main state, which is consistent with the n-type transport behavior of the $Pb_{1-x}Ga_xTe$ compounds. The XPS results further corroborate that Ga is an amphoteric dopant in $Pb_{1-x}Ga_xTe$ with Ga^{3+} as the dominant donor state while Ga^{1+} forms a deep level impurity that ionizes at high temperatures.

Figure 3a shows powder X-ray diffraction (p-XRD) patterns for $Pb_{1-x}Ga_xTe$ (x = 0–0.035) ingots after ice quenching in water. The samples with $x \leq 0.03$ are single-phase compounds with a cubic rock salt structure, within the XRD sensitivity. For samples with $x > 0.03$, a small amount of a secondary phase $PbGa_6Te_{10}$ is detected. The calculated lattice parameter shown in Figure 3b decreases almost linearly with the increasing content of Ga up to 0.03, indicating that Ga successfully substitutes on the Pb site, consistent with the previous results.[13] In the sample with the Ga content of 0.035, the lattice parameter increases due to the presence of the secondary phase $PbGa_6Te_{10}$ (because it removes Ga from the PbTe matrix). Figure 3c shows infrared absorption spectra for $Pb_{1-x}Ga_xTe$. After doping with Ga, the bandgap is almost unchanged in the range from 0.26 to 0.28 eV (Figure S1, Supporting Information). Figure 3d shows the room-temperature carrier concentration as a function of the Ga content for $Pb_{1-x}Ga_xTe$ compounds. The carrier concentration initially increases with increasing Ga content but the concentration is far below the ideal line representing a fully ionized state. Then, with a further increase in Ga, the carrier concentration becomes almost constant at $\approx 1 \times 10^{19}$ cm^{-3}.

© 2018 WILEY-VCH Verlag GmbH & Co. KGaA, Weinheim

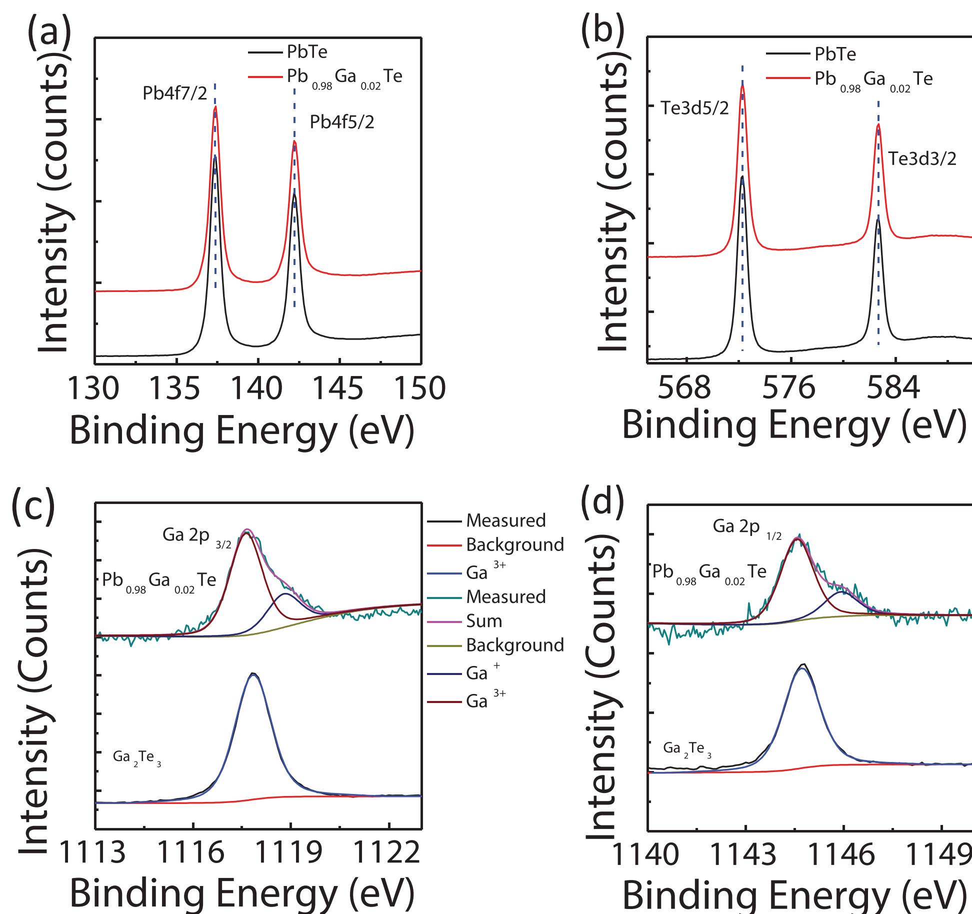

Figure 2. X-ray photoelectron spectra of a) Pb $4f_{7/2}$ and $4f_{5/2}$ core states in $Pb_{1-x}Ga_xTe$ (x = 0, 0.02) samples; b) Te $3d_{5/2}$ and $3d_{3/2}$ core states in $Pb_{1-x}Ga_xTe$ (x = 0, 0.02) samples; c) Ga $2p_{3/2}$ core states in $Pb_{0.98}Ga_{0.02}Te$ and Ga_2Te_3 samples; and d) Ga $2p_{1/2}$ core states in $Pb_{0.98}Ga_{0.02}Te$ and Ga_2Te_3 samples. Ga $2p_{3/2}$ core states and Ga $2p_{1/2}$ core states in the Ga_2Te_3 sample are plotted for comparison to verify the amphoteric role of Ga in the $Pb_{0.98}Ga_{0.02}Te$ compound.

This is well known to occur in the Ga-doped PbTe system[13,14] and is referred to as Fermi level pinning. As suggested by electronic band structure calculations and XPS analysis, a mixture of trivalent Ga^{3+} and monovalent Ga^{+} states stabilizes the Fermi level, leading to the unchanged carrier concentration. Doping with Ga induced the deep level impurity states which trapped the free electron, therefore pinning the Fermi level below the conduction band minimum.[14a,15] The same phenomenon has been observed with other Group III elements (e.g., In) doped into PbTe that form a mixture of trivalent and monovalent states.[11,16]

Figure 4 displays the temperature dependence of the electrical conductivity, Seebeck coefficient, and power factor of $Pb_{1-x}Ga_xTe$ (x = 0–0.035) samples. For Ga contents up to 0.02, the electrical conductivity increases in the entire temperature range as the content of Ga increases. Above x = 0.02, the electrical conductivity slightly decreases. Specifically, the room temperature electrical conductivity increases significantly from 54 S cm^{-1} for the $Pb_{0.995}Ga_{0.005}Te$ sample to 1943 S cm^{-1} for the $Pb_{0.98}Ga_{0.02}Te$ sample. Except for the $Pb_{0.995}Ga_{0.005}Te$ sample, all other samples behave as highly degenerate semiconductors with their electrical conductivity decreasing as the temperature increases. In contrast, the sample with the Ga content of 0.005 displays a typical nondegenerate semiconducting behavior as the electrical conductivity increases with the increasing temperature and approaches the maximum value of 134 S cm^{-1} at 685 K. At higher temperatures, the electrical conductivity decreases. Upon further careful examination of the temperature-dependent electrical conductivity of samples with $x > 0.005$, the transport behavior can be divided into three regimes, depending on the temperature range: The first regime covers temperatures below 570 K, the second regime describes the behavior between 570 and 750 K, and the third regime corresponds to temperatures above 750 K. At the lowest temperatures, below 570 K, the electrical conductivity decreases very rapidly with the increasing temperature. In the second regime, between 570 and 750 K, the rate of decrease in the electrical conductivity becomes very slow and the conductivity is almost flat. For some samples, such as $Pb_{0.99}Ga_{0.01}Te$, the electrical conductivity even slightly increases with the increasing temperature. Above 750 K, the electrical conductivity resumes its larger rate of decrease as the temperature increases. The three regimes essentially coincide with the three regimes shown in the temperature-dependent Hall coefficient for Ga-doped $Pb_{1-x}Ga_xTe$. In the first regime, the Hall coefficient is almost constant, behaving as a highly degenerate semiconductor,

© 2018 WILEY-VCH Verlag GmbH & Co. KGaA, Weinheim

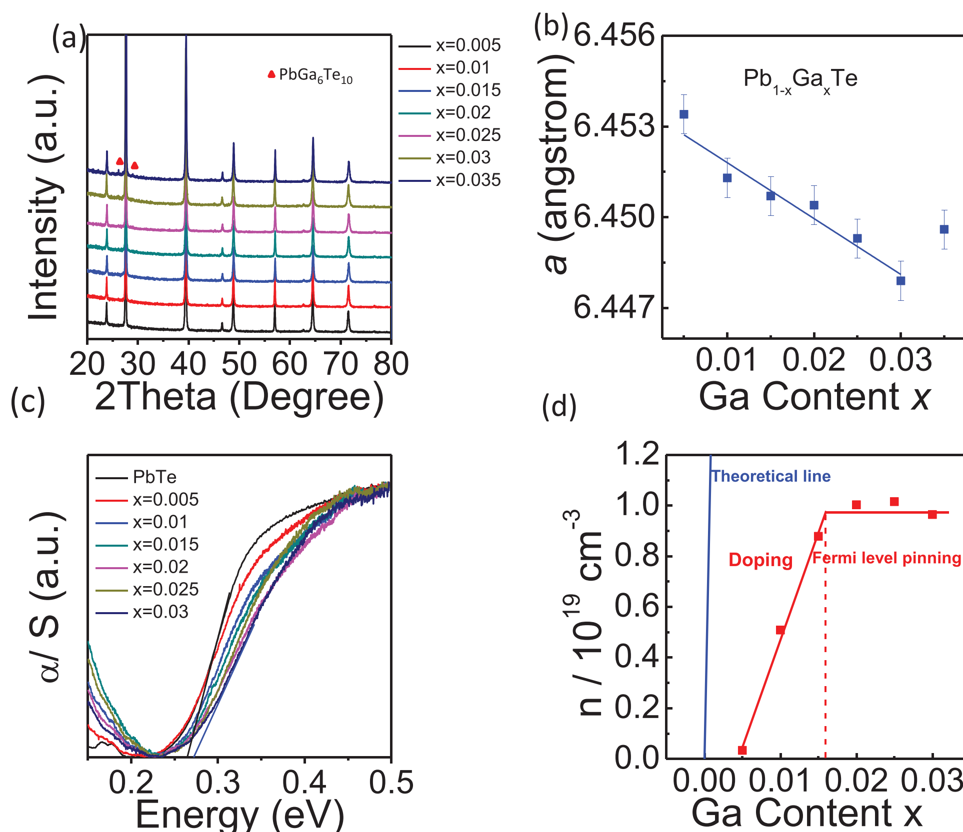

Figure 3. a) XRD patterns of $Pb_{1-x}Ga_xTe$ (x = 0–0.035) compounds after annealing; b) lattice parameter a of $Pb_{1-x}Ga_xTe$ (x = 0–0.035) compounds as a function of Ga content, 0.01% error bars are applied. The solid line is a fit of the lattice parameter according to Vegard's law; c) infrared absorption spectra for $Pb_{1-x}Ga_xTe$ (x = 0–0.03) compounds; d) room-temperature carrier concentration as a function of Ga content. The solid blue line is the calculated carrier concentration assuming that all Ga^{3+} states are fully ionized and donate one electron to the $Pb_{1-x}Ga_xTe$ (x = 0–0.03) system. The red line is a fitted line for guidance to the eye.

whereas in the second regime, the deep level impurity that trapped electrons at the low temperature releases them for charge transport. In the third regime, the onset of intrinsic excitation starts to take over where the electron and hole pair participates in the charge transport. All these produce the slope changes in the σ versus T curve.

The temperature dependence of the Seebeck coefficient of $Pb_{1-x}Ga_xTe$ (x = 0–0.035) samples is shown in Figure 4b. The Seebeck coefficients of all samples are negative in the entire measured temperature range, indicating an n-type transport with electrons as the dominant charge carriers. Further increasing the content of Ga dopant, the absolute value of the Seebeck coefficient decreases for all samples. Specifically, the room-temperature Seebeck coefficient decreases significantly from −356 µV K^{-1} for the $Pb_{0.995}Ga_{0.005}Te$ sample to −125 µV K^{-1} for the $Pb_{0.97}Ga_{0.03}Te$ sample. Except for $Pb_{0.995}Ga_{0.005}Te$, the absolute value of the Seebeck coefficient increases as the temperature increases. For the $Pb_{0.995}Ga_{0.005}Te$ sample, the absolute value of the Seebeck coefficient initially increases with the rising temperature, approaches the maximum value of −387 µV K^{-1} at 385 K, and then decreases with further increase of the temperature. Clearly, the temperature-dependent Seebeck coefficient shows an inverse correlation with respect to the temperature dependence of the electrical conductivity, and could also be divided into three regimes based on the rate with which the magnitude changes with temperature due to the presence of deep level impurity states. A combination of high electrical conductivity and large Seebeck coefficients results in high power factor $\alpha^2\sigma$ of the $Pb_{1-x}Ga_xTe$ compounds in the entire measured temperature range (see Figure 4c). At room temperature, the maximum power factor of 34.9 µW cm^{-1} K^{-2} is achieved with the $Pb_{0.99}Ga_{0.01}Te$ sample, while the $Pb_{0.98}Ga_{0.02}Te$ sample possesses a high power factor of over 20 µW cm^{-1} K^{-2} in a very wide temperature range from 300 to 767 K. Such power factors are much higher than those achieved in other n-type PbTe doped on the cation site[7a,17] with, for example, Sb, Bi, Cd, Zn, La, etc., as shown in Figure 4d.

To reveal the underlying physical mechanism for these extraordinary electronic transport properties, we modeled the Seebeck coefficient and electrical conductivity, assuming a simple parabolic band model and charge carrier scattering dominated by acoustic phonons

$$\alpha = -\frac{k_B}{e} \times \left[\left(r + \frac{5}{2} \right) - \xi \right] \tag{1}$$

$$\sigma = 2e \left(\frac{2\pi m_0 k_B T_0}{h^2} \right)^{\frac{3}{2}} \left(\frac{T}{T_0} \right)^{\frac{3}{2}} \left(\frac{m^*}{m_0} \right)^{\frac{3}{2}} \mu \exp(\xi) \tag{2}$$

© 2018 WILEY-VCH Verlag GmbH & Co. KGaA, Weinheim

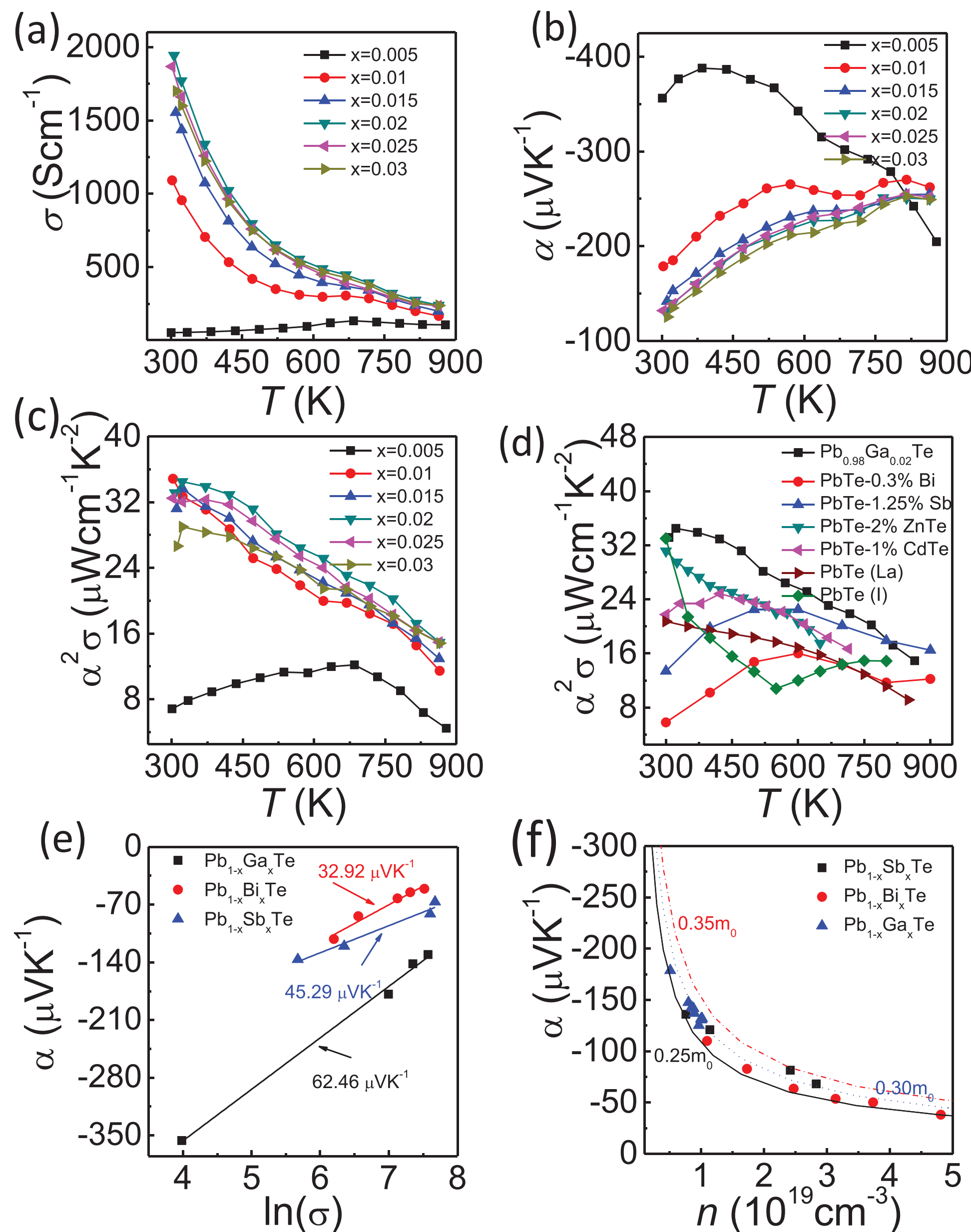

Figure 4. Temperature dependence of the electronic transport properties of $Pb_{1-x}Ga_xTe$: a) electrical conductivity; b) Seebeck coefficient; c) power factor; d) comparison of power factors of PbTe doped with various dopants.[7a,17,19a] e) Room-temperature Seebeck coefficient as a function of the natural logarithm of the electrical conductivity for $Pb_{1-x}Ga_xTe$. High-performance Bi-doped PbTe and Sb-doped PbTe are plotted for comparison.[7a] f) Room-temperature Seebeck coefficient as a function of carrier concentration n for $Pb_{1-x}Ga_xTe$. The black solid line, the blue dotted line, and the red dashed line are the theoretical Pisarenko plots with the effective mass of 0.25, 0.30, and 0.35 m_0, respectively.

Here, k_B, m^*, ξ, r, T_0, e and m_0 are the Boltzmann constant, the effective mass, the reduced Fermi level, the scattering factor, a reference temperature, the elementary electron charge, and the free electron mass, respectively. Combining the above two equations yields an expression for the Seebeck coefficient as a function of the electrical conductivity in the form

$$\alpha = -\frac{k_B}{e} \times \left[C + \frac{3}{2}\ln\left(\frac{T}{T_0}\right) + \ln(U) - \ln(\sigma) \right] \quad (3)$$

where C is equal to 17.71+r and is related to the scattering factor, and U is the weighted mobility defined as $\left(\frac{m^*}{m_0}\right)^{\frac{3}{2}}\mu$. According to the above equation, for a given material system, the value of the partial derivative $\frac{\partial_\alpha}{\partial_{\ln\sigma}}$ should be equal to $\frac{k_B}{e} \approx$ 86.2 μV K^{-1}.

Figure 4e displays the relationship between the room-temperature Seebeck coefficient of samples $Pb_{1-x}Ga_xTe$ and the natural logarithm of the electrical conductivity. For comparison, the relationships for $Pb_{1-x}Bi_xTe$ and $Pb_{1-x}Sb_xTe$ compounds

© 2018 WILEY-VCH Verlag GmbH & Co. KGaA, Weinheim

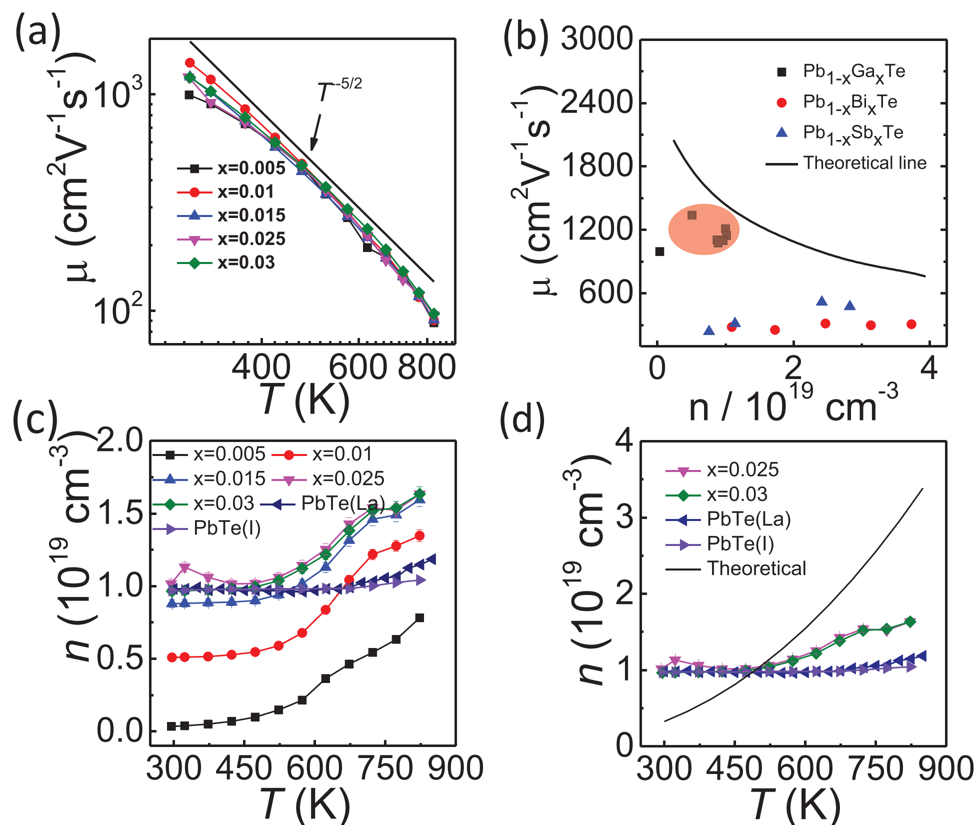

Figure 5. a) Temperature dependence of the carrier mobility for $Pb_{1-x}Ga_xTe$. The black solid line is the trend line with the $T^{-5/2}$ dependence. b) Room-temperature carrier mobility as a function of carrier concentration compared with that of Bi-doped and Sb-doped PbTe.[17a] c) Temperature dependence of the carrier concentration for $Pb_{1-x}Ga_xTe$. Temperature-dependent carrier concentrations for n-type La-doped PbTe[7a] and I-doped PbTe having the room temperature carrier concentration of 1×10^{19} cm^{-3} are plotted for comparison. d) Temperature dependence of the carrier concentration for $Pb_{1-x}Ga_xTe$ ($x = 0.025, 0.03$). Temperature-dependent carrier concentration for n-type La-doped PbTe[7a] and I-doped PbTe both with the room-temperature carrier concentration of 1×10^{19} cm^{-3} are plotted for comparison. The black solid line is the temperature dependence of the optimum carrier concentration calculated by the equation $n^* = 3.25(T/300)^{2.25} \times 10^{18}$ cm^{-3} with a stabilized reduced Fermi level of $\xi = 0.3$, according to the single Kane band model.[7a] Clearly, the carrier concentrations of Ga-doped PbTe are closer to the optimal concentration than in the case of La-[7a] and I-doped PbTe.

are also plotted.[17a] For $Pb_{1-x}Ga_xTe$, the slope is ≈62.5 μV K^{-1}, while the slopes for $Pb_{1-x}Bi_xTe$ and $Pb_{1-x}Sb_xTe$ compounds are ≈32.9 and ≈45.3 μV K^{-1}, respectively. Notably, all the values deviate significantly from the classical value of 86.2 μV K^{-1}, indicating that doping with Sb, Bi, or Ga considerably affects the weighted mobility, that is, the carrier effective mass and the carrier mobility. Assuming energy independence of the carrier mean free path, the Seebeck coefficient of a degenerate semiconductor can be expressed by the following equation

$$\alpha = -\frac{8\pi^2 k_B^2}{3eh^2} m^* T \left(\frac{\pi}{3n}\right)^{\frac{2}{3}} \tag{4}$$

where n is the Hall carrier concentration. Room-temperature values of the Seebeck coefficient as a function of the Hall carrier concentration, the so-called Pisarenko plot, are shown in Figure 4f. It is evident that the carrier concentration dependent Seebeck coefficient can be well described by a single parabolic band (SPB) model with the electron effective mass m^* of about 0.30 m_0 at room temperature for all Sb-, Bi-, and Ga-doped PbTe. Thus, doping with Bi, Sb, and Ga does not change the shape of the band structure near the band edge. However, as noted above, doping with Ga, Sb, or Bi impacts the weighted mobility,[6a] which is determined by the effective mass and the carrier mobility. Consequently, doping PbTe with Ga, Sb, or Bi exerts a strong influence on the carrier mobility. Using the measured Hall coefficient and the electrical conductivity, we have calculated the temperature-dependent carrier mobility, $\mu = R_H\sigma$, which is shown in **Figure 5**a. The Hall mobility for $Pb_{1-x}Ga_xTe$ (x = 0–0.035) compounds decreases very rapidly with the increasing temperature, following a trend line of $T^{-5/2}$, characteristic of the dominance of acoustic phonon scattering in the whole temperature range.[18]

To shed light on the effect of Ga doping on the carrier mobility, the relationship between the carrier mobility and the carrier concentration is plotted in Figure 5b, together with some literature data for PbTe doped with Bi and Sb.[17a] The theoretical line, assuming a single parabolic band and the dominant acoustic phonon scattering, is also indicated by a solid line in Figure 5b. As the carrier concentration increases, the carrier mobility decreases due to enhanced carrier–carrier scattering. At room temperature, the carrier mobility of $Pb_{1-x}Ga_xTe$ is around 1000–1300 cm^2 V^{-1} s^{-1}, while the carrier mobility of $Pb_{1-x}Sb_xTe$ and $Pb_{1-x}Bi_xTe$ compounds is only about 300–500 cm^2 V^{-1} s^{-1}

© 2018 WILEY-VCH Verlag GmbH & Co. KGaA, Weinheim

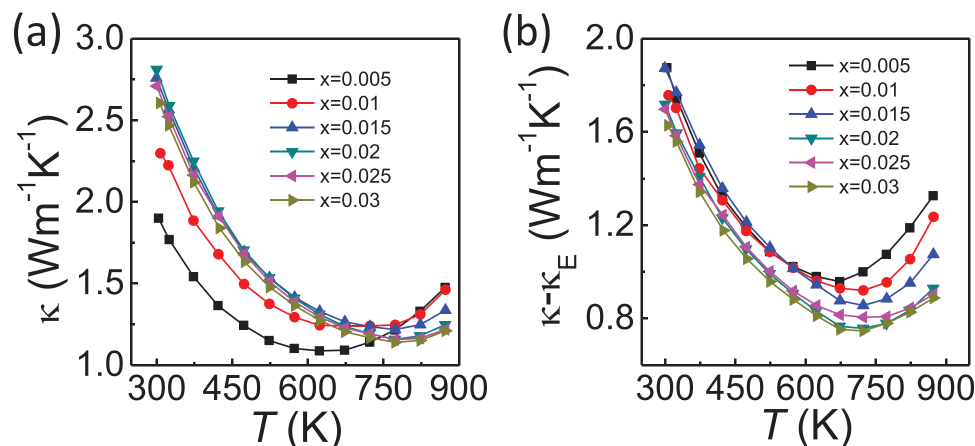

Figure 6. a) Temperature dependence of the thermal conductivity of $Pb_{1-x}Ga_xTe$ compounds; b) temperature dependence of the lattice thermal conductivity of the same $Pb_{1-x}Ga_xTe$ compounds. The onset of bipolar conduction above about 650 K is vividly demonstrated.

for a comparable level of doping. Obviously, the carrier mobility of $Pb_{1-x}Ga_xTe$ compounds is much higher than that of $Pb_{1-x}Sb_xTe$ and $Pb_{1-x}Bi_xTe$ compounds with similar carrier concentrations, indicating a much weaker scattering of charge carriers in Ga-doped samples.

Moreover, the power factor of n-type PbTe is also strongly related to the carrier concentration. With increasing temperature, the required optimum carrier concentration to maximize the power factor increases. Ioffe suggested that the optimum carrier concentration n^* is proportional to $(m^*T)^{3/2}$, where m^* is the density of states effective mass.[7b] Later, Pei et al. proposed that the optimum carrier concentration for n-type PbTe should obey the equation $[n^* = 3.25(T/300)^{2.25} \times 10^{18}\ \text{cm}^{-3}]$ with a stabilized reduced Fermi level of $\xi = 0.3$, according to a single band Kane band model (SKB) and having acoustic (nonpolar) phonon scattering as the dominant phonon scattering mechanism.[7a] Figure 5c shows the temperature dependence of the carrier concentration for Ga-doped $Pb_{1-x}Ga_xTe$ compounds. For comparison, the temperature dependence of carrier concentration for high-performance La- doped PbTe[7a] and I-doped PbTe having similar room-temperature carrier concentrations as $Pb_{0.98}Ga_{0.02}Te$ is also shown. As mentioned earlier, with the increased Ga content, the room-temperature carrier concentration increases and saturates at $\approx 1 \times 10^{19}$ cm^{-3}. It is evident that the carrier concentrations of La- doped PbTe[7a] and I-doped PbTe are essentially independent of temperature, the compounds behaving as highly degenerate semiconductors, except at temperatures above 723 K, where the carrier concentration starts to increase due to the onset of intrinsic excitations. In the case of Ga-doped PbTe, however, the comparable large carrier concentration is roughly constant in the temperature interval of 300–473 K, but then it increases sharply above 523 K as the deep impurity Ga^{1+} levels become ionized. Subsequently, in the temperature interval of 723–823 K, the carrier concentration keeps on increasing but at a slower rate due to the onset of intrinsic excitations.

Assuming that doping with La, I, or Ga does not change the conduction and valence band edges, we can reasonably associate the rapid increase in the carrier concentration of $Pb_{1-x}Ga_xTe$ compounds in the temperature interval of 473–723 K with the ionization of deep level Ga^{1+} impurity states. These deep impurity levels created by Ga^{1+} are obviously activated at a lower temperature than is the onset of intrinsic excitations, as one would expect. As shown in Figure 5d, the presence of the deep level impurity in Ga-doped $Pb_{1-x}Ga_xTe$ compounds can allow the engineering of the temperature dependence of the carrier concentration to values closer to the optimum, plotted as a solid line in Figure 5d. Although not perfect, the carrier concentration in Ga-doped PbTe is much closer to the optimal concentration over a broad range of temperatures than what is typically achieved in La-[7a] and I-doped PbTe, the two reference materials where only shallow impurity levels are present. This results in much higher power factors of Ga-doped PbTe in comparison to other n-type-doped PbTe structures, as documented in Figure 4d. It is worth mentioning that the room-temperature power factor of $Pb_{0.99}Ga_{0.01}Te$ is higher than the power factors of our other Ga-doped $Pb_{1-x}Ga_xTe$ samples due to the relatively low optimum carrier concentration required at room temperature.

2.2. Thermal Conductivity and Figure of Merit *ZT*

The temperature dependence of the total thermal conductivity of $Pb_{1-x}Ga_xTe$ compounds is shown in **Figure 6**a. As the temperature increases, the thermal conductivity of all samples decreases due to enhanced Umklapp phonon–phonon scattering. The thermal conductivity reaches its minimum value between 650 and 800 K, depending on the carrier concentration, and then it precipitously increases with the increasing temperature on account of the onset of intrinsic excitations, which give rise to a strong ambipolar thermal conductivity term.[7b] A notable enhancement in the total thermal conductivity with the greater content of Ga is associated with the increased contribution of charge carriers to the thermal transport. Overall, the total thermal conductivity consists of the electronic thermal conductivity κ_e, the lattice thermal conductivity κ_l, and the ambipolar thermal conductivity κ_{bi}. The electronic thermal conductivity κ_e can be estimated by the Wiedemann–Franz relation, $\kappa_e = L\sigma T$, where σ is the electrical conductivity

© 2018 WILEY-VCH Verlag GmbH & Co. KGaA, Weinheim

and L is the Lorenz number. Assuming a single parabolic band model and transport dominated by acoustic phonon scattering, the Lorenz number L can be calculated from

$$L=\left(\frac{k_B}{e}\right)^2\left(\frac{(r+7/2)F_{r+5/2}(\eta)}{(r+3/2)F_{r+1/2}(\eta)}-\left[\frac{(r+5/2)F_{r+3/2}(\eta)}{(r+3/2)F_{r+1/2}(\eta)}\right]^2\right) \quad (5)$$

where k_B is the Boltzmann constant, e is the electron charge, r is the scattering factor (here, again, $r = -1/2$), η is the reduced Fermi energy, and $F_n(\eta)$ is the Fermi integral defined as

$$F_n(\eta)=\int_0^\infty \frac{\chi^n}{1+e^{\chi-\eta}}d\chi \quad (6)$$

Using the calculated temperature-dependent Lorenz number and the Wiedemann–Franz law, we can calculate $\kappa_l + \kappa_{bi}$, which is shown in Figure 6b

$$\kappa_l+\kappa_{bi}=\kappa-L\sigma T \quad (7)$$

The room-temperature lattice thermal conductivity of the $Pb_{0.995}Ga_{0.005}Te$ compound is about 1.88 W m^{-1} K^{-1}. As the content of Ga increases, the lattice thermal conductivity decreases to 1.63 W m^{-1} K^{-1} measured for the $Pb_{0.97}Ga_{0.03}Te$ compound. The decrease is likely due to enhanced point defect phonon scattering, given that the Ga doping within the PbTe matrix is up to 3 at%, according to the XRD results. As the temperature increases, the lattice thermal conductivity decreases, following the trend in the total thermal conductivity, until the onset of intrinsic excitations, at which point the rapidly rising ambipolar thermal conductivity term takes over. From the data in Figure 6b, it follows that the enhanced carrier concentration in more heavily Ga-doped PbTe assists in shifting the onset of intrinsic excitations to higher temperatures. The $Pb_{0.97}Ga_{0.03}Te$ compound possesses the lowest lattice thermal conductivity of 0.75 W m^{-1} K^{-1} at 723 K.

The presence of deep impurity Ga^{1+} states together with shallow impurity Ga^{3+} states is very effective in enhancing the power factor in Ga-doped $Pb_{1-x}Ga_xTe$ compounds over a wide temperature range. Coupled with the reduced thermal conductivity, the Ga-doped PbTe compounds attain high ZT values of as much as 1.34 at 766 K, shown in **Figure 7**a, which is comparable with other single-doped PbTe (Figure 7b).[7a,17a,19] More importantly, the much superior power factor, particularly at temperatures below 650 K, results in a record-high average ZT value of 1.03 for $Pb_{0.98}Ga_{0.02}Te$ over the temperature range from 300 to 865 K and an even higher average ZT value of 1.12 for $Pb_{0.98}Ga_{0.02}Te$ over the temperature range from 420 to 865 K. This average ZT value is considerably higher than in the

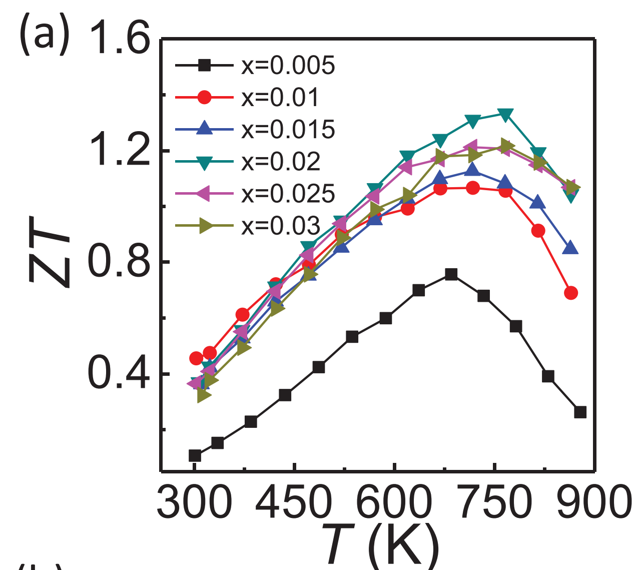

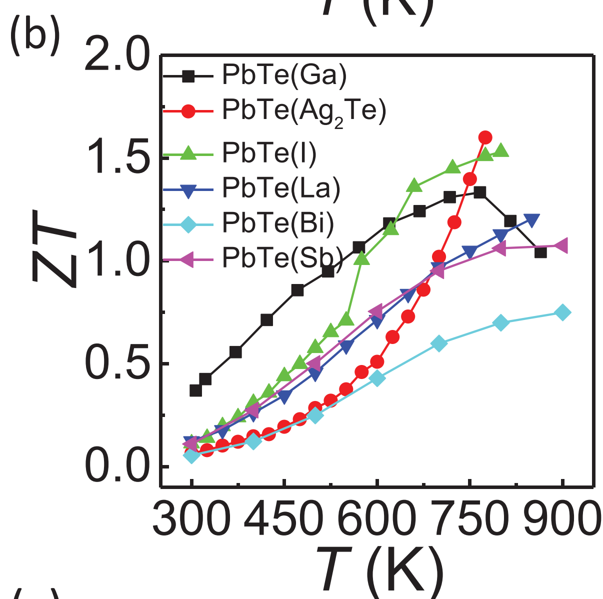

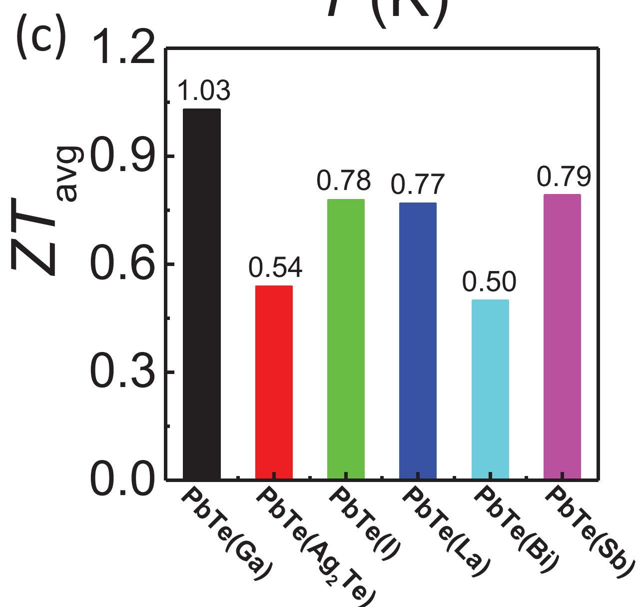

Figure 7. Temperature dependence of electronic transport properties of $Pb_{1-x}Ga_xTe$: a) ZT value; b) comparison of ZT values with high-performance n-type $PbTe(Ag_2Te)$, I-doped PbTe, La-doped PbTe, Bi-doped PbTe, and Sb-doped PbTe.[7a,17a,19] Clearly, the present Ga-doped PbTe is superior up to temperatures of about 600 K. c) Comparison of the average ZT in the measured temperature range with the same compounds as in (b). Ga-doped PbTe achieves a record-high average ZT in excess of unity over the interval from 300 to 865 K.

© 2018 WILEY-VCH Verlag GmbH & Co. KGaA, Weinheim

previous studies of PbTe with dopants, such as I, Sb, Bi, and La (Figure 7c).[7a,17a,19]

3. Conclusions

In this work, we have documented the amphoteric doping nature of Ga in $Pb_{1-x}GaTe$. Combining first principles calculations with experimental investigations, we have shown that doping Ga into PbTe gives rise to two kinds of impurity states: shallow levels associated with the Ga^{3+} state and deep levels due to the Ga^{1+} state. The presence of deep Ga^{1+}-derived levels allows us to engineer the carrier concentration to match more closely the optimum carrier concentration required for maximizing the power factor over a wide temperature range. Furthermore, Ga doping surprisingly weakens electron–phonon scattering, leading to large carrier mobilities observed in Ga-doped PbTe compounds. At the same time, Ga doping decreases the lattice thermal conductivity as it enhances point defect phonon scattering. As a consequence, a peak ZT of 1.34 at 766 K and the record-high average ZT of 1.03 were obtained in the temperature range of 300–865 K. Our work provides a new avenue for optimizing the performance of thermoelectric materials beyond the conventional shallow level doping. We think that by exploring dual-role dopants that can form both shallow and deep impurity level states, the power factor of many materials can be improved over a broad range of temperatures.

4. Experimental Section

Synthesis: High-purity elements: Ga (shot, 99.99%, Sigma-Aldrich, USA), Pb (wire, 99.99%, American elements, USA), and Te (shot, 99.999%, Canada) were weighed and mixed according to the nominal composition of $Pb_{1-x}Ga_xTe$ (x = 0–0.035). Stoichiometric quantities of the elements were sealed in evacuated quartz tubes and slowly heated up to 1373 K and held at this temperature for 24 h. Subsequently, the ampoules were furnace cooled down to 873 K and held there for 48 h and then quenched in ice water to room temperature. For a typical experiment, the following amounts were used: Pb (9.1728 g, 44.27 mmol), Te (5.7642 g, 45.17 mmol), and Ga (0.0630 g, 0.90 mmol) to prepare a 15 g ingot of $Pb_{0.98}Ga_{0.02}Te$.

Densification: The obtained ingots were hand-ground into fine powders using a mortar and a pestle. The powder was then sintered by spark plasma sintering (SPS) at 823 K under a pressure of 40 MPa in a vacuum to obtain fully densified bulk samples.

XRD and XPS: The phase structure of samples was examined by powder XRD analysis (Rigaku Miniflex powder diffractometer, Cu$K\alpha$). XPS of PbTe and $Pb_{0.98}Ga_{0.02}Te$ was conducted on a Thermo Scientific ESCALAB 250 Xi spectrometer equipped with a monochromatic Al $K\alpha$ X-ray source (1486.6 eV) operating at 300 W. Samples were analyzed under ultrahigh vacuum ($P < 10^{-8}$ mbar) with a pass energy of 150 eV (survey scans) or 25 eV (high-resolution scans). All peaks were calibrated with C 1s peak binding energy at 284.7 eV. The experimental peaks were fitted with Avantage software.

Thermoelectric Properties: The electrical conductivity and the Seebeck coefficient were measured at the same time using the ZEM-3 (Ulvac Riko, Inc.) apparatus under a helium atmosphere from 300 to 873 K. The thermal conductivity was calculated according to the relationship $\kappa = DC_p\rho$, where D, C_p, and ρ are the thermal diffusivity, the heat capacity, and the density of bulk samples, respectively. The thermal diffusivity (D) was measured using the laser flash system (LFA 457; Netzsch) in an argon atmosphere (Figure S2, Supporting Information). The heat capacity (C_p) as shown in Figure S2 (Supporting Information) is estimated from the relation C_p/k_b per atom = 3.07 + (4.7 × 10^{-4} × (T–300)), and the sample density (ρ) was calculated by using the mass of the samples and their dimensions (Table S1, Supporting Information).

Hall Measurements: The high-temperature Hall measurements were performed in a home-made apparatus in an argon atmosphere. The Hall resistance was monitored with a Linear Research ac resistance bridge (LR-700) operated at 17 Hz, and the data were taken in a field of ±0.5 T provided by an air-bore Oxford superconducting magnet. The carrier concentration n and the carrier mobility μ_H were calculated according to equations: $n = 1/eR_H$ and $\mu_H = \sigma R_H$.

Band Structure Calculations: The total energies and relaxed geometries of Ga-doped PbTe with a 54 atom cell ($Pb_{26}GaTe_{27}$) were calculated by density functional theory (DFT) within the generalized gradient approximation (GGA) of the Perdew–Burke–Ernzerhof exchange-correlation functional with projector augmented wave potentials.[20] Periodic boundary conditions and a plane wave basis set as implemented in the Vienna ab initio simulation package were used.[21] The total energies were numerically converged to ≈3 meV/cation using a basis set energy cutoff of 500 eV and dense k-meshes corresponding to 4000 k-points per reciprocal atom in the Brillouin zone. Due to the heavy atomic species, the spin–orbit coupling effects were considered in the band structure calculations.

Supporting Information

Supporting Information is available from the Wiley Online Library or from the author.

Acknowledgements

The authors wish to acknowledge support from the Natural Science Foundation of China (Grant Nos. 51521001, and 51632006). At Northwestern University (X.S., S.H., C.W., and M.G.K.), synthesis, thermoelectric property measurements and band structure calculations were supported by a grant from the U.S. Department of Energy, Office of Science, and Office of Basic Energy Sciences under Award No. DE-SC0014520.

Conflict of Interest

The authors declare no conflict of interest.

Keywords

deep level impurities, Ga doping, PbTe, thermoelectric properties

Received: February 27, 2018
Revised: April 1, 2018
Published online: May 16, 2018

[1] a) G. Tan, L. D. Zhao, M. G. Kanatzidis, *Chem. Rev.* **2016**, *116*, 12123; b) X. Su, P. Wei, H. Li, W. Liu, Y. Yan, P. Li, C. Su, C. Xie, W. Zhao, P. Zhai, Q. Zhang, X. Tang, C. Uher, *Adv. Mater.* **2017**, *29*, 1602013; c) J. He, T. M. Tritt, *Science* **2017**, *357*, 1369; d) W. G. Zeier, A. Zevalkink, Z. M. Gibbs, G. Hautier, M. G. Kanatzidis, G. J. Snyder, *Angew. Chem., Int. Ed.* **2016**, *55*, 6826.
[2] a) L. D. Zhao, G. Tan, S. Hao, J. Q. He, Y. Pei, H. Chi, H. Wang, S. Gong, H. Xu, V. P. Dravid, C. Uher, G. J. Snyder, C. Wolverton,

 © 2018 WILEY-VCH Verlag GmbH & Co. KGaA, Weinheim

M. G. Kanatzidis, *Science* **2016**, *351*, 141; b) Y. Zheng, Q. Zhang, X. Su, H. Xie, S. Shu, T. Chen, G. Tan, Y. Yan, X. Tang, C. Uher, G. J. Snyder, *Adv. Energy Mater.* **2015**, *5*, 1401391; c) G. Tan, F. Shi, J. W. Doak, H. Sun, L. D. Zhao, P. Wang, C. Uher, C. Wolverton, V. P. Dravid, M. G. Kanatzidis, *Energy Environ. Sci.* **2015**, *8*, 267; d) G. J. Tan, F. Y. Shi, S. Q. Hao, L. D. Zhao, H. Chi, X. M. Zhang, C. Uher, C. Wolverton, V. P. Dravid, M. G. Kanatzidis, *Nat. Commun.* **2016**, *7*, 12167; e) X. Shi, J. Yang, J. R. Salvador, M. Chi, J. Y. Cho, H. Wang, S. Bai, J. Yang, W. Zhang, L. Chen, *J. Am. Chem. Soc.* **2011**, *133*, 7837.

[3] a) T. Liang, X. Su, Y. Yan, G. Zheng, X. She, Y. You, C. Uher, M. G. Kanatzidis, X. Tang, *NPG Asia Mater.* **2017**, *9*, e352; b) H. Xie, X. Su, Y. Yan, W. Liu, L. Chen, J. Fu, J. Yang, C. Uher, X. Tang, *NPG Asia Mater.* **2017**, *9*, e390; c) D. Yang, X. Su, Y. Yan, T. Hu, H. Xie, J. He, C. Uher, M. G. Kanatzidis, X. Tang, *Chem. Mater.* **2016**, *28*, 4628; d) H. Xie, X. Su, G. Zheng, T. Zhu, K. Yin, Y. Yan, C. Uher, M. G. Kanatzidis, X. Tang, *Adv. Energy Mater.* **2016**, *7*, 1601299; e) G. Zheng, X. Su, X. Li, T. Liang, H. Xie, X. She, Y. Yan, C. Uher, M. G. Kanatzidis, X. Tang, *Adv. Energy Mater.* **2016**, *6*, 1600595.

[4] a) M. K. Jana, K. Pal, A. Warankar, P. Mandal, U. V. Waghmare, K. Biswas, *J. Am. Chem. Soc.* **2017**, *139*, 4350; b) M. Samanta, S. Roychowdhury, J. Ghatak, S. Perumal, K. Biswas, *Chem. Eur. J.* **2017**, *23*, 7438; c) A. Banik, B. Vishal, S. Perumal, R. Datta, K. Biswas, *Energy Environ. Sci.* **2016**, *9*, 2011; d) A. Banik, U. S. Shenoy, S. Saha, U. V. Waghmare, K. Biswas, *J. Am. Chem. Soc.* **2016**, *138*, 13068; e) K. Biswas, J. He, I. D. Blum, C. I. Wu, T. P. Hogan, D. N. Seidman, V. P. Dravid, M. G. Kanatzidis, *Nature* **2012**, *489*, 414; f) K. Biswas, J. Q. He, Q. Zhang, G. Wang, C. Uher, V. P. Dravid, M. G. Kanatzidis, *Nat. Chem.* **2011**, *3*, 160; g) Z. W. Chen, Z. Z. Jian, W. Li, Y. J. Chang, B. H. Ge, R. Hanus, J. Yang, Y. Chen, M. X. Huang, G. J. Snyder, Y. Z. Pei, *Adv. Mater.* **2017**, *29*, 1606768; h) D. Wu, L. D. Zhao, X. Tong, W. Li, L. J. Wu, Q. Tan, Y. L. Pei, L. Huang, J. F. Li, Y. M. Zhu, M. G. Kanatzidis, J. Q. He, *Energy Environ. Sci.* **2015**, *8*, 2056; i) L. D. Zhao, H. J. Wu, S. Q. Hao, C. I. Wu, X. Y. Zhou, K. Biswas, J. Q. He, T. P. Hogan, C. Uher, C. Wolverton, V. P. Dravid, M. G. Kanatzidis, *Energy Environ. Sci.* **2013**, *6*, 3346; j) L. D. Zhao, S. H. Lo, J. He, H. Li, K. Biswas, J. Androulakis, C. I. Wu, T. P. Hogan, D. Y. Chung, V. P. Dravid, M. G. Kanatzidis, *J. Am. Chem. Soc.* **2011**, *133*, 20476; k) X. Su, H. Li, G. Wang, H. Chi, X. Zhou, X. Tang, Q. Zhang, C. Uher, *Chem. Mater.* **2011**, *23*, 2948; l) G. Zheng, X. Su, H. Xie, Y. Shu, T. Liang, X. She, W. Liu, Y. Yan, Q. Zhang, C. Uher, M. G. Kanatzidis, X. Tang, *Energy Environ. Sci.* **2017**, *10*, 2638; m) X. Su, F. Fu, Y. Yan, G. Zheng, T. Liang, Q. Zhang, X. Cheng, D. Yang, H. Chi, X. Tang, Q. Zhang, C. Uher, *Nat. Commun.* **2014**, *5*, 4908.

[5] D. G. Cahill, S. K. Watson, R. O. Pohl, *Phys. Rev. B* **1992**, *46*, 6131.

[6] a) Y. Pei, X. Shi, A. LaLonde, H. Wang, L. Chen, G. J. Snyder, *Nature* **2011**, *473*, 66; b) W. Liu, X. Tan, K. Yin, H. Liu, X. Tang, J. Shi, Q. Zhang, C. Uher, *Phys. Rev. Lett.* **2012**, *108*, 166601; c) J. P. Heremans, C. M. Thrush, D. T. Morelli, *Phys. Rev. B* **2004**, *70*, 115334; d) J. P. Heremans, V. Jovovic, E. S. Toberer, A. Saramat, K. Kurosaki, A. Charoenphakdee, S. Yamanaka, G. J. Snyder, *Science* **2008**, *321*, 554.

[7] a) Y. Z. Pei, Z. M. Gibbs, A. Gloskovskii, B. Balke, W. G. Zeier, G. J. Snyder, *Adv. Energy Mater.* **2014**, *4*, 1400486; b) A. F. Ioffe, *Semiconductor Thermoelements, and Thermoelectric Cooling*, Infosearch, London **1957**; c) S. Hui, W. P. Gao, X. Lu, A. Panda, T. P. Bailey, A. A. Page, S. R. Forrest, D. T. Morelli, X. Q. Pan, K. P. Pipe, C. Uher, *Adv. Energy Mater.* **2018**, *8*, 1701623.

[8] a) Q. C. Song, J. W. Zhou, L. Meroueh, D. Broido, Z. F. Ren, G. Chen, *Appl. Phys. Lett.* **2016**, *109*, 263902; b) H. G. Grimmeiss, *Annu. Rev. Mater. Sci.* **1977**, *7*, 341.

[9] S. Wang, J. Yang, T. Toll, J. Yang, W. Zhang, X. Tang, *Sci. Rep.* **2015**, *5*, 10136.

[10] K. Lischka, *Phys. Status Solidi B* **1986**, *133*, 15.

[11] S. Ahmad, K. Hoang, S. D. Mahanti, *Phys. Rev. Lett.* **2006**, *96*, 056403.

[12] Q. Zhang, E. K. Chere, Y. M. Wang, H. S. Kim, R. He, F. Cao, K. Dahal, D. Broido, G. Chen, Z. F. Ren, *Nano Energy* **2016**, *22*, 572.

[13] E. P. Skipetrov, E. A. Zvereva, O. S. Volkova, E. I. Slyn'ko, A. M. Mousalitin, *Mater. Sci. Eng., B* **2002**, *91*, 416.

[14] a) D. E. Dolzhenko, V. N. Demin, I. I. Ivanchik, D. R. Khokhlov, *Semiconductors* **2000**, *34*, 1144; b) E. P. Skipetrov, O. V. Kruleveckaya, L. A. Skipetrova, E. I. Slynko, V. E. Slynko, *Appl. Phys. Lett.* **2014**, *105*, 022101; c) Z. Feit, D. Eger, A. Zemel, *Phys. Rev. B* **1985**, *31*, 3903.

[15] A. I. Belogorokhov, B. A. Volkov, I. I. Ivanchik, D. R. Khokhlov, *JETP Lett.* **2000**, *72*, 123.

[16] K. Hoang, S. D. Mahanti, *Phys. Rev. B* **2008**, *78*, 085111.

[17] a) G. Tan, C. C. Stoumpos, S. Wang, T. P. Bailey, L. D. Zhao, C. Uher, M. G. Kanatzidis, *Adv. Energy Mater.* **2017**, *7*, 1700099; b) K. Ahn, M. K. Han, J. Q. He, J. Androulakis, S. Ballikaya, C. Uher, V. P. Dravid, M. G. Kanatzidis, *J. Am. Chem. Soc.* **2010**, *132*, 5227; c) P. K. Rawat, B. Paul, P. Banerji, *ACS Appl. Mater. Interfaces* **2014**, *6*, 3995.

[18] a) Y. I. Ravich, B. A. Efimova, V. I. Tamarchenko, *Phys. Status Solidi B* **1971**, *43*, 453; b) Y. Z. Pei, A. D. LaLonde, H. Wang, G. J. Snyder, *Energy Environ. Sci.* **2012**, *5*, 7963.

[19] a) A. D. LaLonde, Y. Z. Pei, G. J. Snyder, *Energy Environ. Sci.* **2011**, *4*, 2090; b) Y. Z. Pei, J. Lensch-Falk, E. S. Toberer, D. L. Medlin, G. J. Snyder, *Adv. Funct. Mater.* **2011**, *21*, 241.

[20] J. P. Perdew, K. Burke, M. Ernzerhof, *Phys. Rev. Lett.* **1996**, *77*, 3865.

[21] G. Kresse, J. Furthmuller, *Phys. Rev. B* **1996**, *54*, 11169.

© 2018 WILEY-VCH Verlag GmbH & Co. KGaA, Weinheim